American Mineralogist, Volume 87, pages 47–55, 2002

Electron paramagnetic resonance spectroscopic study of synthetic fluorapatite: Part II. Gd^{3+} at the Ca1 site, with a neighboring Ca2 vacancy

NING CHEN,[1] YUANMING PAN,[1,*] JOHN A. WEIL,[2] AND MARK J. NILGES[3]

[1]Department of Geological Sciences, University of Saskatchewan, Saskatoon, Saskatchewan S7N 5E2, Canada
[2]Department of Chemistry, University of Saskatchewan, Saskatoon, Saskatchewan S7N 5C9, Canada
[3]Illinois EPR Research Center, University of Illinois, Urbana, Illinois 61801, U.S.A.

ABSTRACT

A W-band (94 GHz) electron paramagnetic resonance (EPR) study of synthetic fluorapatite with 57 ± 4 ppm Gd has been made on single crystals at ~287 K. The spectra disclosed the presence of a previously unreported type of Gd^{3+} center denoted by "b" herein (S = 7/2), in addition to the Gd^{3+} center "a" assigned to the Ca2 site using the results of a previous X-band (9.5 GHz) EPR study (Chen et al. 2002). In particular, the single-crystal W-band EPR spectra from three orthogonal-rotation planes allowed determination of an appropriate spin-Hamiltonian for center "b," including the spin terms of type BS (matrix **g**) and S^2 (matrix **D**) and the parameters associated with the high-spin terms of type S^4 and S^6 as well as BS^3 and BS^5. Agreement between the observed and simulated single-crystal spectra confirmed the validity of the spin-Hamiltonian analysis.

The principal values of the matrices **g** and **D** [e.g., $D/g_e\beta_e$ = 1069.2(1) G and $E/g_e\beta_e$ = 52.4(3) G] suggest a considerably distorted rhombic local environment for the Gd^{3+} ions in center "b." The principal directions of **D** suggest that "b" corresponds to Gd^{3+} at the Ca1 site. This site assignment is supported by a pseudo-symmetry analysis of the term S^4, i.e., approximate matching of the directions of the calculated pseudo-symmetry axes to the bond directions and face normals of the coordination polyhedron of the ideal Ca1 site. The data suggest that the incorporation of Gd^{3+} into the Ca1 site is achieved by a coupled substitution ($2Gd^{3+} + \square \leftrightarrow 3Ca^{2+}$) involving a Ca^{2+} vacancy $\square$ and that the vacancy is located at a next-nearest-neighbor Ca2 site, resulting in a Gd^{3+}- - $\square$ - - - Gd^{3+} arrangement, with the cations well separated.

INTRODUCTION

In a previous contribution (Chen et al. 2002), we reported the results of an X-band (9.4 GHz) electron paramagnetic resonance (EPR) spectroscopic study of synthetic fluorapatite containing 1.2 ± 0.2 wt% [~10 000 ppm] Gd_2O_3, and described a Gd^{3+} center "a" assigned to the Ca2 site (Fig. 1). That study provided information for the local structural environment of the Gd^{3+} ion in that site, complementing data from high-precision X-ray structure refinement of natural and synthetic REE-bearing apatites (e.g., Hughes et al. 1991; Fleet and Pan 1995; Comodi et al. 1999; Fleet et al. 2000a, 2000b). Moreover, the local structural environment of the Gd^{3+} ion in "a" furnished insight into the substitution mechanism for incorporating this ion (as a representative of the trivalent rare-earth elements, REEs) into the Ca2 site in fluorapatite. The X-band EPR spectra also suggested the possible presence of another major Gd^{3+} center ("b"), which at this frequency is only partly observed in the single-crystal spectra. Center "b" is the primary subject of the present paper.

The present study was initiated for two reasons. Firstly, a new synthesis experiment was conducted to produce fluorapatite single crystals containing only approximately ~100 ppm Gd to take advantage of the EPR technique for investigating this paramagnetic ion at trace levels of concentration, such as are commonly encountered in natural apatites (e.g., Pan et al. 1993; Pan and Breaks 1997). Second, the single-crystal EPR study was performed at the more energetic and sensitive W-band frequency (~94 GHz) in order to investigate the Gd^{3+} center "b" that was only partly observed in the X-band experiments, to determine the spin-Hamiltonian parameters for "b." The fitted spin-Hamiltonian parameters together with a pseudo-symmetry analysis using the S^4 parameters in turn permitted a detailed evaluation of the local structural environment of the Gd^{3+} ion in "b." In particular, these results showed that Gd^{3+} of the center "b" corresponds to substitution into the Ca1 site, which has a different stereochemical environment from the Ca2 site (Fig. 1; cf., Hughes et al. 1989). Moreover, information about the Gd^{3+} ion in "b" provided insight into a different mechanism of substitution for incorporating REEs into fluorapatite, which (unlike that for the Gd^{3+} center "a" at the Ca2 site) appears to involve a vacancy. The results reported herein also allowed an independent testing for the spin-Hamiltonian of the Gd^{3+} center "a" obtained from the X-band study (Chen et al. 2002).

* E-mail: yuanming.pan@usask.ca

0003-004X/02/0001–47$05.00

Brought to you by | University of Toronto-Ocul
Authenticated
Download Date | 12/1/15 12:10 PM

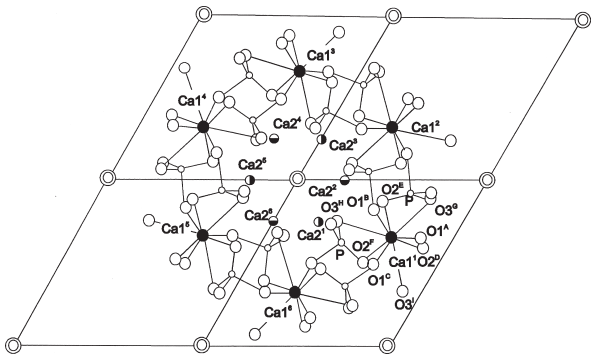

FIGURE 1. The (001) projection of the fluorapatite structure (after Hughes et al. 1989); note the symmetry-related Ca1 sites (labeled from $Ca1^1$ to $Ca1^6$) and Ca2 sites ($Ca2^1$, $Ca2^3$, and $Ca2^5$ at z = 1/4; whereas $Ca2^2$, $Ca2^4$, and $Ca2^6$ are at z = 3/4). Also labeled are the nine nearest-neighbor oxygen atoms (from $O1^A$ to $O3^I$) of $Ca1^1$.

TABLE 1. Ideal and calibrated directions of the rotation-plane normals and the crystal reference systems used in the W-band EPR experiments

Plane	x (or x')		y (or y')		z (or z')	
	θ (°)	φ (°)	θ (°)	φ (°)	θ (°)	φ (°)
xy	90.00^A	0.00^A			0.00^N	0.00^N
x'y'	92.72^A	15.14^A			5.00^N	52.22^N
yz	90.00^N	180.00^N			0.00^A	0.00^A
x'y'	89.48^N	179.98^N			0.54^A	14.40^A
xz			90.00^N	90.00^N	0.00^A	0.00^A
x'y'			89.78^N	90.22^N	0.22^A	95.59^A

Notes: ^{A} = Axis directions; ^{N} = Nornal directions of the rotation planes.

EXPERIMENTAL METHODS

Synthesis and characterization of fluorapatite crystals

The synthesis of the Gd-doped fluorapatite single crystals of this study was similar to that described in Chen et al. (2002), except that the starting material contained only approximately 100 ppm Gd rather than ~10 000 ppm Gd. The experimental product, including the size, morphology and optical properties of the fluorapatite crystals, was similar to that described in Chen et al. (2002). X-ray fluorescence microprobe analysis at the University of Saskatchewan (cf., Cheburkin et al. 1997), using other Gd-doped fluorapatite crystals that have been analyzed by electron microprobe and laser-ablation inductively coupled plasma mass spectrometry (Fleet and Pan 1997; Chen et al. 2002) as standards, revealed that the synthetic fluorapatite crystal of this study contains 57 ± 4 ppm Gd.

EPR experiments

Single-crystal EPR spectra of the Gd-doped fluorapatite were obtained at ~287 K on the MARK II W-band (94 GHz) EPR spectrometer (Nilges et al. 1999) at the Illinois EPR Research Center (IERC), University of Illinois at Urbana-Champaign. As in the previous single-crystal X-band experiments (Chen et al. 2002), field-swept W-band EPR experiments were performed with the Zeeman field **B** in three orthogonal rotation planes. The deviations of the actual experimental system x'y'z' from the ideal experimental system xyz are estimated in Table 1 (see Chen et al. 2002 for the definition of the reference system). Precise alignment of single crystals with respect to **B** (e.g., Chen et al. 1999) is relatively difficult on the W-band instrument owing in part to its small resonant cavity (~2.4 mm in diameter). In this study, we mounted a prismatic crystal of the Gd-doped fluorapatite in a quartz tube of 0.7 mm internal diameter, which was then aligned inside the resonant cavity under binoculars for field-swept measurements in plane x'y' (i.e., $\mathbf{B} \perp \mathbf{z}'$). For measurements in the planes x'z' and y'z', the crystal of fluorapatite was mounted using Duco cement on a quartz rod (0.78 mm diameter), which was glued directly to the resonant cavity using such cement. Alignment was made approximately by use of a well-developed crystal face and a crystal edge of the hexagonal prism as references for x'z' and y'z', respectively. Not surprisingly, relatively large errors in crystal alignment existed (e.g., ~15° in the x'y' plane; Table 1). These errors were corrected for initially according to the line-position roadmaps in the three orthogonal rotations and were corrected further during the spin-Hamiltonian optimization by using the software package EPR-NMR (Mombourquette et al. 1996). Figure 2 shows the line-position roadmaps of the three rotations in the ideal experimental system. The validity of the calibrations of the crystal alignment has been confirmed by excellent agreement between the observed and predicted single-crystal spectra of "a" from all transitions of the Gd^{3+} ions (S = 7/2) at the six symmetry-related Ca2 sites when **B**||**z**', as well as by agreement between the observed and calculated single-crystal spectra for selected transitions (e.g., between spin-projection quantum numbers m_S: –1/2 and +1/2) when **B**||**x**' and when **B**||**y**'.

The field-swept EPR experiments with the Zeeman field **B** rotated in the three orthogonal planes were carried out at average frequencies 94.467(8), 94.480(3), and 94.460(8) GHz for planes x'y', x'z', and y'z', respectively (Figs. 2 and 3). The spectral resolution was 4.9 G (i.e., 4096 field data points over 20 000 G in each spectrum), and the angle intervals were 10° and 20° in plane x'y', and 10° in the x'z' and y'z' planes. The numbers of line-position data points were 163, 234, and 254 in planes x'y', x'z', and y'z', respectively. The B-field calibration of the W-band spectrometer was done by use of a Metrolab NMR Teslameter PT2025 (Nilges et al. 1999). The standard deviations of the line-position errors between the observed values and those obtained from the spin-Hamiltonian parameters for center "b" were found to be 13 G (15 lines), 11 G (16 lines), and 10 G (7 lines) at **B**||**x**', **B**||**y**', and **B**||**z**', respectively. The actual field calibration was made by comparison, for center "a," of the observed line positions in the W-band experiments and those predicted by the spin-Hamiltonian parameters derived from the well-calibrated X-band experiments (Chen et al. 2002). The standard deviations of the line-position errors for "b" were thereby reduced to 7, 5, and 3 G at **B**||**x**', **B**||**y**', and **B**||**z**', respectively.

Powder samples of the Gd-doped fluorapatite were obtained by grinding single crystals in an agate mortar, and were investigated on the MARK II W-band EPR spectrometer at ~287 K

Brought to you by | University of Toronto-Ocul
Authenticated
Download Date | 12/1/15 12:10 PM

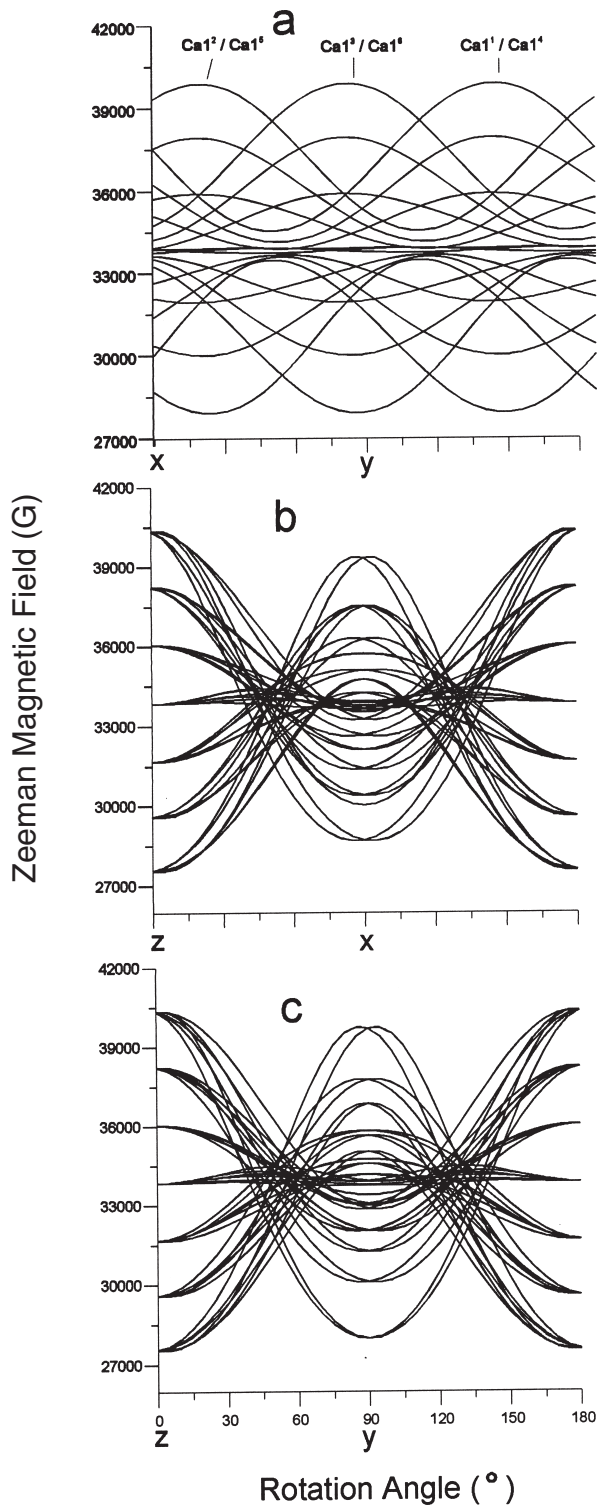

FIGURE 2. Angular dependence ("roadmaps") of the EPR spectra predicted by the obtained spin-Hamiltonian for the Gd^{3+} center "b," with the Zeeman field **B** rotated in planes for the ideal experimental system: (**a**) xy; (**b**) xz; and (**c**) yz. Note that in the plane xy, each curve is twofold degenerate. The six calcium sites are magnetically equivalent at **B**||**z**.

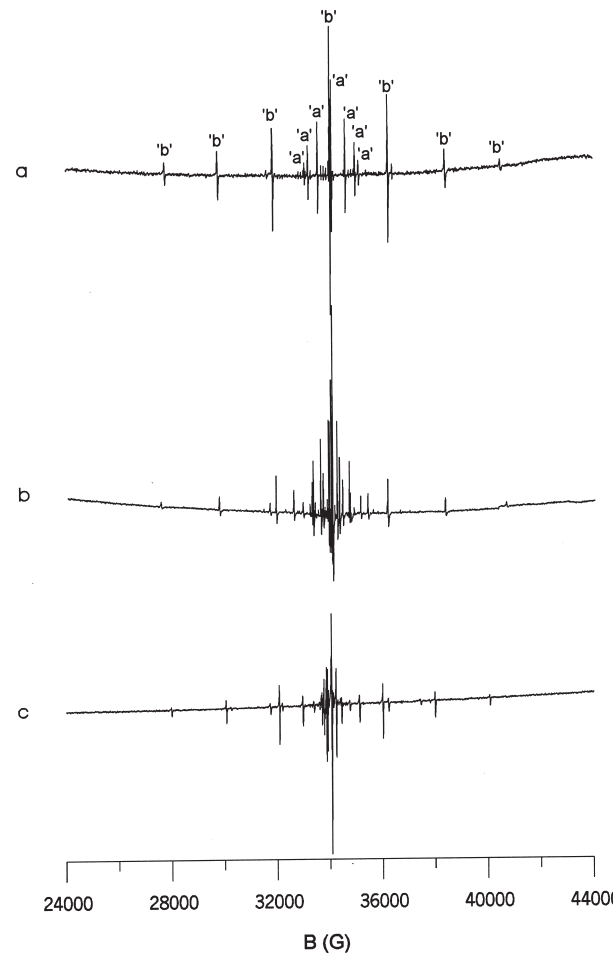

FIGURE 3. Single-crystal W-band EPR spectra of the Gd-doped fluorapatite at ~287 K: (**a**) **B**||**z**' with $\mathbf{B}_1$||**x**', at ν = 94.5017 GHz; note that lines related to the Gd^{3+} center "b" are labeled as "b" and those for the Gd^{3+} center "a" at the Ca2 sites as "a"; (**b**) **B**||**x**' with $\mathbf{B}_1$||**y**', at ν = 94.4682 GHz; (**c**) **B**||**y**' and $\mathbf{B}_1$||**x**', at ν = 94.4579 GHz. Note that magnetic site splittings are visible when **B**||**x**' and **B**||**y**'.

and on a Q-band (~35 GHz) Varian E-15 EPR spectrometer at ~295K. The powder W-band spectrum shows that, except for the very strong central peak (transition $-1/2 \leftrightarrow +1/2$), the signals from the other transitions are not well defined. The powder Q-band spectrum shows better resolution for the other transitions but, as was shown by simulation, is dominated by contributions from center "a."

RESULTS AND DISCUSSION

EPR spectra

The single-crystal W-band EPR spectra of the Gd-doped fluorapatite consist of two distinct centers ("a" and "b") of Gd^{3+} (S = 7/2). The first one corresponds to Gd^{3+} located at the Ca2 sites, which has been investigated in detail in the previous X-band EPR study (Chen et al. 2002). The EPR signals from center "b" are clearly detected in the W-band spectra and are characterized by a larger fine-structure splitting than that of

Brought to you by | University of Toronto-Ocul
Authenticated
Download Date | 12/1/15 12:10 PM

the Gd^{3+} ions at the Ca2 sites. As discussed below, the Gd^{3+} ions of the center "b" can be assigned to being at Ca1 sites.

Figure 3a shows that the spectral fine-structures of the Gd^{3+} centers "a" and "b" in fluorapatite are clearly observed at W-band spectra for **B**||**z**'. The seven anisotropic lines assigned to "b" are from its primary "allowed" transitions (Fig. 4). The lines from the "forbidden" transitions (Fig. 4) were shown by simulation using the final spin-Hamiltonian to be very weak (≤0.01% of the "allowed" transitions for both centers), and thus were not measured.

At field orientations other than **B**||**z**', magnetic-site splittings from Gd^{3+} in the six symmetry-related sites $Ca1^{i}$ (i = 1, 2, …, 6; Fig. 1) shown as the multiple line structure for any given transition are well resolved for center "b." The presence of the three seven-line fine structures (twofold degenerate, Fig. 2a) in the ideal rotation plane xy indicates a C_3 effective proper rotation group, which is a subgroup of the actual C_6 crystal-symmetry proper-rotation group (Fig. 1). Furthermore the spectra are strongly angular dependent, and crossovers of the EPR transitions occur in the spectra in all three rotations (Fig. 2).

The W-band EPR spectra do not show any evidence of hyperfine structure for either of the two Gd^{3+} centers, as was also noted in the X-band experiments (Chen et al. 2002). We attribute this primarily to the low natural abundances of ^{155}Gd and ^{157}Gd relative to their even isotopic counterparts. Simulation for each of the individual lines of "b" at **B**||**z**', where no magnetic-site splittings are visible (see below), yielded no evidence for the presence of any satellite hyperfine peaks.

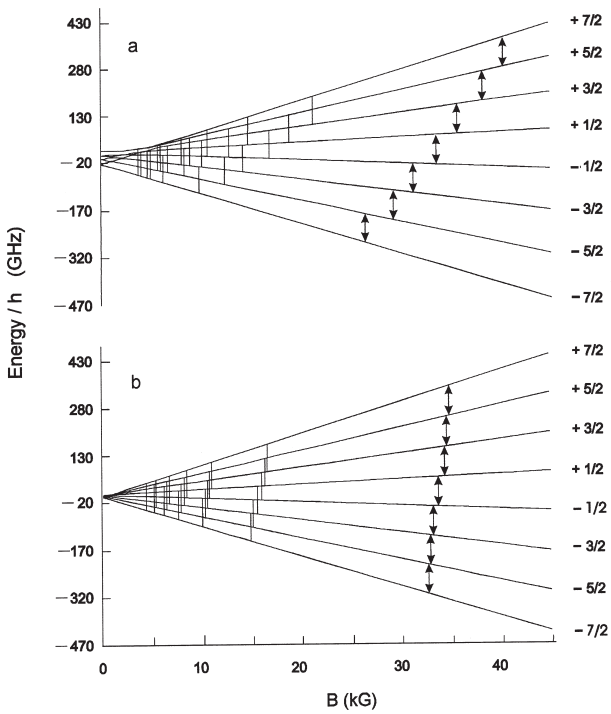

FIGURE 4. Simulated energy levels when **B**||**z** for the two types of the Gd^{3+} centers in fluorapatite: (**a**) the center "b"; and (**b**) the center "a" at $Ca2^{1}$. The seven "allowed" transitions for the two centers, at ν = 94.5017 GHz and T = ~287 K, are labeled as lines with arrows (length = ν). The lines without arrows in the lower magnetic regions indicate "forbidden" transitions at the same frequency and temperature, which have not been observed. The spin-projection quantum numbers (m_S) are labeled on the right.

EPR line shapes and line widths

The basic EPR line shape for center "b" is of the Lorentzian type, as confirmed by simulation for the seven EPR spectral lines with **B**||**z**' and excitation field $\mathbf{B}_1$||**x**' (Fig. 5). The estimated deviation between **z** and **z**' was 0.22°. As stated, the Gd^{3+} ions at the six symmetry-related Ca1 sites (Fig. 1) contribute as many as 6 distinct "symmetry-related" EPR lines for each transition. At **B**||**z**, the 6 lines are superimposed (full degeneracy).

At **B**||**z**', near degeneracy is expected. This has been confirmed by the observed spectrum (Fig. 5), which indicated the approximate superposition of the 6 "symmetry-related" EPR lines (i.e., transition between m_S: –1/2 ↔ +1/2) arising from the symmetry-related Ca1 sites. The single-crystal spectrum simulation (Fig. 5) revealed that the 6 lines are actually three-fold doubly degenerate (with spacings 0.51 and 0.54 G, and internal splittings of 0.18, 0.14, and 0.05 G, respectively), resulting in a total broadening effect of 1.3 G, i.e., a line broadening effect of such a magnitude. Since the measured line width is 12.5 G (including the unresolved broadening effect arising from the magnetic site splitting), the inherent EPR line width, observable at **B**||**z**, will be approximately 10.2 G. Possible

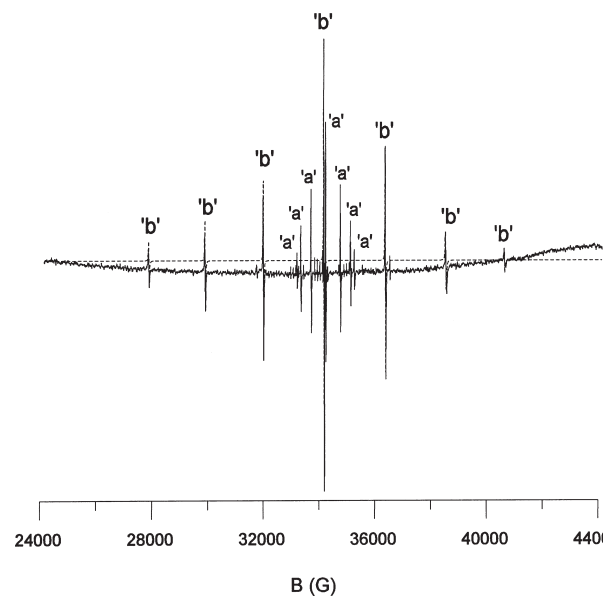

FIGURE 5. Observed (solid line) and simulated (dashed line) single-crystal EPR spectra of Gd^{3+} in fluorapatite with **B**||**z**' and $\mathbf{B}_1$||**x**', at ν = 94.5017 GHz and T = ~287 K; the Lorentzian line widths used (maxmin of the 1st derivative; in gauss) for the lines from the Gd^{3+} center "b" are 21.5 (–7/2 ↔ –5/2), 18.0 (–5/2 ↔ –3/2), 14.1 (–3/2 ↔ –1/2), 12.5 (–1/2 ↔ +1/2), 14.6 (+1/2 ↔ +3/2), 18.0 (+3/2 ↔ +5/2) and 21.5 (+5/2 ↔ +7/2) at a frequency of 94.5017 GHz, respectively. Note that simulation also included the spectrum of the Gd^{3+} center "a" (Chen et al. 2002) at the Ca2 sites.

Brought to you by | University of Toronto-Ocul
Authenticated
Download Date | 12/1/15 12:10 PM

cause(s) for the inherent line widths of the Gd^{3+} centers have been discussed in Chen et al. (2002).

Analogously, the inherent line width for the Gd^{3+} center "a" at the Ca2 sites was found to be 8.7 G at W-band, which is slightly greater than that (6.4 G) found at X-band (Chen et al. 2002). This difference in observed line width for "a" between W- and X-band experiments may be due to the different spectral resolutions used (i.e., 4.9 and 0.1 G, respectively).

It is worth noting that, in the W-band experiments, the inherent line width for center "b" is 1.5 G broader than that for "a," suggesting additional effect(s) affecting "b." For example, there may exist greater "D-strain," i.e., slight differences in the principal values and directions of the matrices **D** for the two Gd^{3+} ions at Ca1 sites thought to be situated between a nearby vacancy located at a Ca2 site (see below).

At all field orientations other than **B**||**z**, the degeneracy is lifted, i.e., splitting into 2, 3, or 6 lines occurs but is not necessarily detectable. Hence an effective line width greater than the inherent one is generally observed. This too has been confirmed by simulations of the central lines ($-1/2 \leftrightarrow +1/2$), including all 6 magnetic sites. In plane xy, the roadmap (Fig. 2a) as well as the simulations of the single-crystal spectra indicate twofold degeneracy for each of the three separated line sets.

At **B**||**x** and **B**||**y**, the single-crystal spectrum simulation revealed again that the six components of the central line ($-1/2 \leftrightarrow +1/2$) become 3 doubly degenerate line sets (with spacing of 3.05 and 121.53 G at **B**||**x**, and 24.33 and 129.25 G at **B**||**y**). These calculated spacings indicate that one of the doubly degenerate lines will be completely separated from the lines arising from other symmetry-related Ca1 sites and this makes it possible to estimate the inherent line widths in this plane similar to that done at **B**||**z**'. As stated, our measurements were not taken exactly in the plane xy because of the deviation in the crystal alignment. Additional site splittings occur with **B** away from this plane, resulting in observed line widths (i.e., effective widths) greater than the inherent ones.

With **B** in planes x'z' and y'z', the line widths are anisotropic owing to the (line-position) contributions arising from the different magnetic sites. The measured line width of the central line (transition $-1/2 \leftrightarrow +1/2$) in plane x'z' has a minimum value of 12.5 G at **B**||**z**' but has a higher value of 13.3 G at **B**||**x**', whereas the line widths in plane y'z' are 12.9 and 14.2 G at **B**||**z**' and **B**||**y**', respectively. The simulation for the single-crystal spectra in plane x'z' revealed that the observed effective line widths are proportional to the magnetic site splitting. This result can explain why measured line widths at **B**||**z**' is larger in plane y'z' than those observed in plane x'z' at **B**||**z**'. This difference in line widths is most likely attributable to the considerably larger errors in the crystal alignment for the y'z' plane (Table 1).

The experimental results at W-band indicate that the line widths of center "b" are a function of the transition (between $m_S \leftrightarrow m_S + 1, -7/2 \leq m_S \leq 5/2$), increasing with increasing $|m_S|$. This effect also is seen in the W-band spectra for Gd^{3+} at the Ca2 sites, but is smaller than was observed at X-band (Chen et al. 2002) because of the increased microwave frequency. This observation agrees semi-quantitatively (when D-strain is invoked) with that predicted by the splitting expression derived from the energy equation of second-order perturbation theory (Weil et al. 1994; p. 189).

Spin-Hamiltonian optimization and spectral simulation

Program EPR-NMR (Mombouquette et al., 1996) was used in the optimization of the spin-Hamiltonian parameters for the W-band spectra. On the basis of the magnetic-site splitting observed in plane x'y' (Fig. 2a), the spin-Hamiltonian optimization was attempted first by assuming an effective C_3 symmetry. Subsequently, C_6 symmetry was adopted in fitting to match the actual magnetic crystal symmetry, and the same results were obtained as those generated with C_3. During the course of the optimization, iterative fittings were made separately for each of the spin-Hamiltonian terms [i.e., the BS term (**g** matrix), the S^2 term (**D** matrix), and the terms BS^3, S^4, BS^5, and S^6], and were followed by a simultaneous fitting for all terms and corrections for the directions of the magnetic field. In each step of these fittings, iteration was continued until no changes at the last decimal point (the machine accuracy) of the root-mean-sum-of-squares of weighted differences (RMSD) between the calculated and observed line positions. The same weighting criteria as those used in optimization of the spectra for "a" (Chen et al. 2002) were adopted when optimizing the W-band spectra for "b." The final RMSD for line positions was 7.0 G, which is approximately half of the observed line width of the central line (12.5 G for the transition $-1/2 \leftrightarrow +1/2$) at **B**||**z**'.

The six symmetry-related matrices **g** and **D** for the effective magnetic point group C_6 can be assigned to the six Ca1 sites (Fig. 1). Matrices **g** and **D** for one of the Ca1 sites (i.e., the one labeled $Ca1^1$ in Fig. 1) are given in Tables 2 and 3, and the parameters for the terms of type S^4, S^6, and BS^3 are summarized in Table 4. The contribution from each spin-Hamiltonian term (i.e., Equation 1 in Chen et al. 2002) to the overall RMSD has been evaluated by setting that term to zero while keeping all other terms at the optimized values. The resulting calculated contributions from terms BS^3, S^4, BS^5, and S^6 to the RMSD are 18.47, 21.16, 1.88, and 0.84 G, respectively. The magnitude of the parameters in the term BS^3 is 10^{-5} (Table 4), whereas the magnitude of the parameters in the term BS^5 is 10^{-6} (not included in Table 4). An even smaller magnitude is expected for the parameters in the term BS^7, which therefore were not included in the optimization.

The three principal values of **g** (Table 2), although very close to being identical and slightly smaller than that of a free electron, are distinct and thus indicate rhombic local symmetry. These g values are similar to those of other Gd^{3+} centers (Al'tshuler and Kozyrev 1974; App. I-§14).

Now considering parameter matrix **D**, one notes that the orientation of the principal D_3 axis is almost parallel to the crystallographic **c** axis (Table 3), while those of D_1 and D_2 are close to the directions of two Ca1-O3 bonds (see below), strongly suggesting that the Gd^{3+} ion occupies the Ca1 sites (Fig. 1). Figure 6 shows the directions $\mathbf{D}_1$ and $\mathbf{D}_2$ for the six symmetry-related Gd^{3+}-occupied Ca1 sites. A separate optimization, in which the direction $\mathbf{D}_3$ was forced to be parallel to the axis **z** (i.e., **B**||**c**) and without imposing any other constraints, resulted in a considerably larger RMSD value of 76.7 G, confirming that the deviation of $\mathbf{D}_3$ from **c** is significant. The fact that **g**

Brought to you by | University of Toronto-Ocul
Authenticated
Download Date | 12/1/15 12:10 PM

TABLE 2. The principal values and directions of the matrices **g** for the Gd^{3+} center 'b' at ~ 287 K and the Gd^{3+} center "a" at the $Ca2^1$ site* at 294.8 K

Y	Matrices			k	Principal values Y_k	Principal directions θ_k (°)†	φ_k (°)†
	1.99075(7)	0.00133(5)	–0.00010(6)	1	1.99160(6)	36(3)	37(3)
$\mathbf{g}^{Ca1'}$		1.98686(7)	0.00123(6)	2	1.99098(6)	122(3)	6(7)
			1.99107(3)	3	1.98610(6)	104(1)	106(1)
	1.9914(2)	–0.0003(2)	0.0003(2)	1	1.9916(2)	73(8)	345(7)
$\mathbf{g}^{Ca2'}$ *		1.9900(2)	–0.0003(2)	2	1.9903(2)	14(2) ×10	5(2) ×10
			1.9902(2)	3	1.9898(2)	6(2) ×10	9(1) ×10

Note: The estimated errors are given in parentheses.
* See Part I.
† Relative to the ideal experimental coordinate system.

TABLE 3. The principal values (in magnetic-field units) and directions of the matrices **D** for the Gd^{3+} center "b" at ~287 K and the Gd^{3+} center "a" at $Ca2^1$* at 294.8 K

Center	Matrix $\mathbf{D}/g_e\beta_e$ (G)			k	Principal Values $D_k/g_e\beta_e$ (G)	Principal directions θ_k (°)‡	φ_k (°)‡
	409.0(2)	–300.4(2)	–59.0(2)	1	664.3(2)	87.40(1)	140.01(2)
$Ca1^1$		303.9(2)	30.5(2)	2	51.7(2)	89.06(2)	230.06(2)
			–713.0(1)	3	–716.0(2)	2.73(1)	340.0(3)
	$D/g_e\beta_e$ = 1069.2(1) G, $E/g_e\beta_e$ = 52.4(3) G†						
	67.07(5)	0.06(6)	6.23(7)	1	67.37(6)	88.1(1)	36(8)
$Ca2^{1*}$		67.13(6)	2.83(8)	2	67.06(6)	90.4(3)	125(8)
			–134.19(4)	3	–134.43(4)	1.94(2)	204.4(7)
	$D/g_e\beta_e$ = 201.64(4) G, $E/g_e\beta_e$ = 0.16(6) G †						

* See Part I.
† $D = 3D_3/2$, $E = (D_1 - D_2)/2$ (Weil et al. 1994).
‡ Relative to the ideal experimental coordinate system.

TABLE 4. Parameters of the high-spin terms of type S^4, S^6, and BS^3 at ~287 K for the Gd^{3+} center "b"

S^4 ($l_1 = 0$)		S^6 ($l_1 = 0$)		BS^3 ($l_1 = 1$)		
m_2	$B_{l_2=4}^{m_2}$ (G)	m_2	$B_{l_2=6}^{m_2}$ ×10^{-3} (G)	l	m	$g_{l,m,3}$ ×10^{-5}
0	0.0593(8)	0	–0.36(4)	2	0	2.0(2)
1	–0.10(1)	1	4.4(7)	2	1	–7.0(4)
2	0.067(9)	2	5.0(7)	2	2	–3.8(4)
3	3.31(6)	3	3(2)	2	–1	21.8(6)
4	0.02(1)	4	–5(1)	2	–2	8.8(4)
–1	0.35(1)	5	–2(65)	4	0	–3.3(2)
–2	–0.143(8)	6	3(1)	4	1	–0.9(3)
–3	–1.16(4)	–1	–6.9(8)	4	2	–12.7(4)
–4	–0.53(1)	–2	3(7)	4	3	18.3(5)
		–3	–18(2)	4	4	–10.1(3)
		–4	–9(9)	4	–1	5.9(3)
		–5	–23(7)	4	–2	–14.7(3)
		–6	7(1)	4	–3	–17.3(1)
				4	–4	–12.9(1)

Note: For indices l_1, l_2, l, m_2, and m as well as symbol, $g_{l,m,3}$, see Mombourquette et al. (1986). Also, the conventional Stevens parameters ($B_{l_2=4}^{m_2}$ and $B_{l_2=6}^{m_2}$) as defined in Mombourquette et al. (1986).

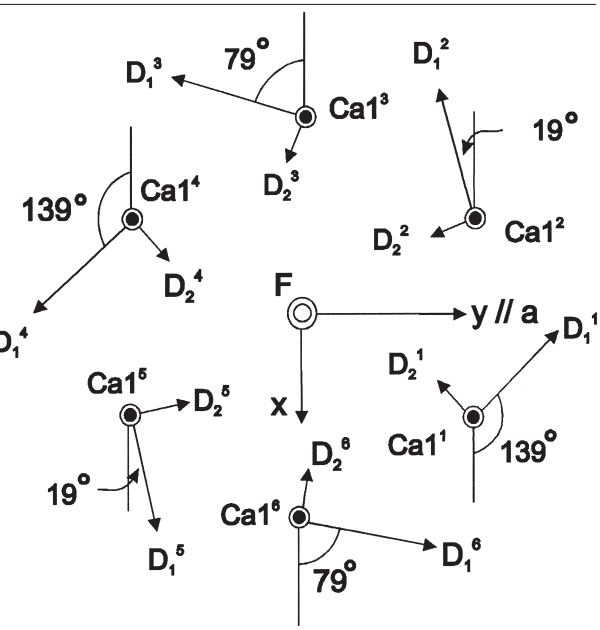

FIGURE 6. Projection along the crystallographic **c** axis of the principal directions of $\mathbf{D}_1$ and $\mathbf{D}_2$ of the six symmetry-related matrices **D** obtained at T = ~287 K for the Gd^{3+} centers "b" located at the six symmetry-related Ca1 sites (see Fig. 1). Note that the sites $Ca1^1$ and $Ca1^4$, $Ca1^2$ and $Ca1^5$, and $Ca1^3$ and $Ca1^6$ are magnetically equivalent at $\mathbf{B}\perp\mathbf{c}$ ($\mathbf{c}\|\mathbf{z}$).

and **D** have different sets of principal directions (Tables 2 and 3) also suggests that the Gd^{3+} ion in center "b" has a low local symmetry.

Figure 4a illustrates that the calculated energy levels at $\mathbf{B}\|\mathbf{z}$ are in close agreement with the results of the W-band EPR experiments. The "allowed" transitions ($|\Delta m_S| = 1$) tend to occupy higher magnetic field regions than do the "forbidden" transitions ($|\Delta m_S| > 1$). The roadmap predicted by the estimated spin-Hamiltonian for the xy plane in the ideal experimental coordinate system clearly shows that there is a threefold symmetry axis along the crystallographic axis **c** (Fig. 2a), and the roadmaps for the xz and yz planes are indicative of sixfold degeneracy at $\mathbf{B}\|\mathbf{z}$ (Figs. 2b and 2c). The observed and simulated single-crystal spectra at $\mathbf{B}\|\mathbf{z}'$ (Fig. 5) and $\mathbf{B}\|\mathbf{x}'$ and $\mathbf{B}\|\mathbf{y}'$ are in excellent agreement, supporting the validity of the calculated spin-Hamiltonian (Tables 2, 3, and 4).

Moreover, the validity of the determined spin-Hamiltonian parameters for "b" and "a" (Chen et al. 2002) has also been

Brought to you by | University of Toronto-Ocul
Authenticated
Download Date | 12/1/15 12:10 PM

demonstrated by the excellent agreement between the observed and simulated Q-band powder spectra (Fig. 7).

Pseudo-symmetry analysis

The assignment of the Gd^{3+} ions of center "b" to the Ca1 sites has been evaluated further by pseudo-symmetry analysis of the fourth-degree term S^4 of the spin-Hamiltonian (e.g., Michoulier and Gaite 1972; Gaite, 1980; 1987; Gaite et al. 1985; Mombourquette et al. 1986), using the program ROTSTO (Tennant et al. 2000), following the method discussed in Chen et al. (2002). Figure 8 summarizes the results of the pseudo-symmetry analysis for "b," in the upper hemisphere ($0 \le \theta \le 90°$, $0 \le \varphi \le 360°$) of a stereographic projection, along with the direction projections for the bonds and face-normals of the coordination polyhedron of the $Ca1^1$ site (Fig.1) calculated from the X-ray data for pure fluorapatite (Hughes et al. 1989).

Two fourfold pseudo-symmetry axes, $\mathbf{F}_4^A$ and $\mathbf{F}_4^B$, were found and match approximately the bonds $Ca1^1$-$O3^I$ and $Ca1^1$-$O2^D$, respectively (Table 5, and Figs. 1 and 8). Four well-defined threefold pseudo-symmetry axes ($\mathbf{F}_3^A$, $\mathbf{F}_3^B$, $\mathbf{F}_3^C$, and $\mathbf{F}_3^D$; Table 5) were found to be located on the great circle (Fig. 8). Axis $\mathbf{F}_3^A$ matches approximately the directions of the bond $Ca1^1$-$O3^G$ (Fig. 1) as well as axis $\mathbf{D}_1$. Axis $\mathbf{F}_3^B$ almost coincides with the direction $\mathbf{D}_2$, and matches approximately the bond $Ca1^1$-$O3^H$ (Fig. 1). Axes $\mathbf{F}_3^C$ and $\mathbf{F}_3^D$ match approximately the normal directions of the faces $O1^A$-$O2^D$-$O3^I$ and $O1^C$-$O2^F$-$O3^I$ (Fig. 1), respectively. Another threefold pseudo-symmetry axis ($\mathbf{F}_3^E$) corresponds approximately to the normal direction of the $O2^E$-$O2^F$-$O3^H$ face (Table 5 and Figs. 1 and 8). A single twofold pseudo-symmetry axis ($\mathbf{F}_2$) was found to be present near the **c** axis (at polar coordinates $\theta = 1°$, $\varphi = 178°$). This pseudo-symmetry axis is inconsistent with the threefold symmetry axis expected for an ideal Ca1 site (cf., Hughes et al. 1989), but its

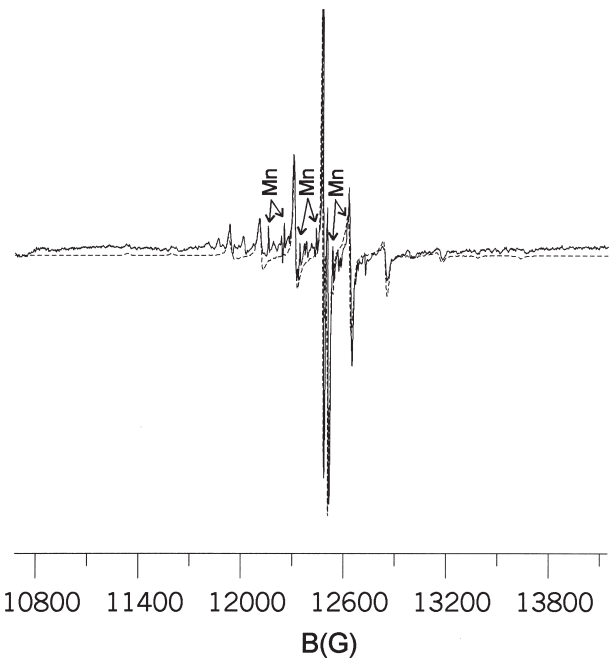

FIGURE 7. Observed (solid line) and simulated (dashed line) Q-band powder EPR spectrum of Gd-doped fluorapatite at the experimental frequency $\nu = 34.7983$ GHz and temperature 298 K. The simulation was made for lorentzian lineshape and various effective line widths for the "allowed" transitions for the centers "a" and "b," with a concentration ratio of the two centers at 3.42 (estimated from the single-crystal W-band spectra, see text). Note that one set of impurity Mn^{2+} sextets is shown explicitly.

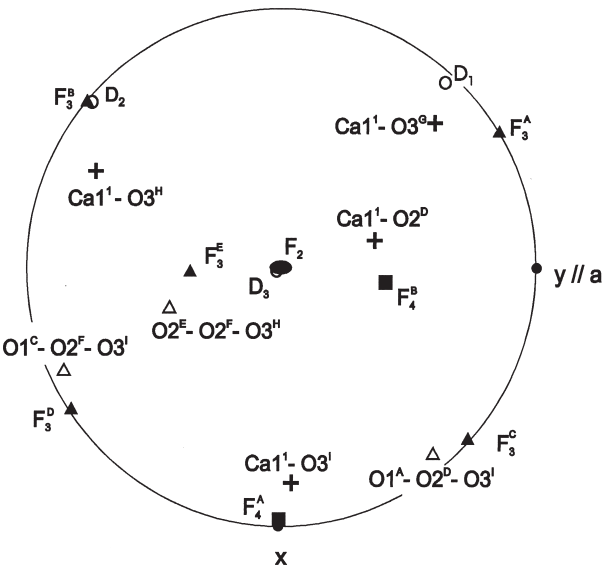

FIGURE 8. Stereographic projection (**c**||**z**) of the calculated pseudo-symmetry axes (solid ellipse, twofold; solid triangles, threefold; solid square, fourfold) of the Gd^{3+} center "b" at the $Ca1^1$ site. Note that the calculated pseudo-symmetry axes [$\mathbf{F}_2$, twofold; $\mathbf{F}_3^i$ (i = A, B, C, D, and E), threefold; $\mathbf{F}_4^j$ (j = A and B)] match closely to the principal directions of the matrix **D** (open circles) selected bonds (pluses) $Ca1^1$-$O2^D$, $Ca1^1$-$O3^I$, $Ca1^1$-$O3^G$, and $Ca1^1$-$O3^H$, and the normal directions of the faces (open triangles) $O1^A$-$O2^D$-$O3^I$, $O1^C$-$O2^F$-$O3^I$, and $O2^E$-$O2^F$-$O3^H$ of the $Ca1^1$ coordination polyhedron (Fig. 1). Also note that the axes of the ideal experimental reference system xyz are indicated by solid circles.

TABLE 5. Comparison of the calculated pseudo-symmetry elements with the principal directions of the matrix **D** of the Gd^{3+} center "b" and with selected bonds and faces of the CaO_9 coordination polyhedron at the $Ca1^1$ site

Pseudo-symmetry elements		Directions θ (°)	φ (°)	Principal D* axes	Directions θ (°)	φ (°)	Ω (°)
$\mathbf{F}_2$	2-fold	1	358	D_3	3	340	2
$\mathbf{F}_3^A$	3-fold	90	123	D_1	87	140	17
$\mathbf{F}_3^B$	3-fold	90	231	D_2	89	230	1
				Bond†			
$\mathbf{F}_3^A$	3-fold	90	123	$Ca1^1$-$O3^G$	80	133	10
$\mathbf{F}_3^B$	3-fold	90	231	$Ca1^1$-$O3^H$	80	253	24
$\mathbf{F}_4^A$	4-fold	89	356	$Ca1^1$-$O3^I$	80	13	19
$\mathbf{F}_4^B$	4-fold	45	88	$Ca1^1$-$O2^D$	45	112	17
				Polyhedron face‡			
$\mathbf{F}_3^C$	3-fold	90	51	$O1^A$-$O2^D$-$O3^I$	88	72	9
$\mathbf{F}_3^D$	3-fold	90	304	$O1^C$-$O2^F$-$O3^I$	88	292	13
$\mathbf{F}_3^E$	3-fold	40	270	$O2^E$-$O2^F$-$O3^H$	50	292	18

Note: Here Ω is the angle between the directions of the pseudo-symmetry elements.
*Directions of the principal D axes.
† Bonds of the site coordination.
‡ Faces of the coordination polyhedron (Fig. 8).

Brought to you by | University of Toronto-Ocul
Authenticated
Download Date | 12/1/15 12:10 PM

existence can be explained by distortion related to the suggested mechanism for incorporating Gd^{3+} into such a site (see below). Therefore, we see that the calculated pseudo-symmetry elements (Fig. 8) correspond closely to selected bonds and faces of the CaO_9 coordination polyhedron at the $Ca1^1$ site (Fig. 1), as well as the principal directions of the matrix **D**, strongly supporting the site assignment of the Gd^{3+} ions of center "b" to the Ca1 sites.

The assignment of the center "b" as arising from Gd^{3+} in site Ca1 is further strengthened by the fact that the local symmetry at the ideal Ca2 site is not consistent with the principal directions of the D matrix or the calculated pseudo-symmetry from the S^4 terms.

The association between Gd^{3+} and a vacancy

A likely mechanism for incorporating Gd^{3+} ions into the Ca1 sites in the synthetic fluorapatite is: $2Gd^{3+} + \square \leftrightarrow 3Ca^{2+}$ (i.e., a Gd^{3+} -- $\square$ --- Gd^{3+} arrangement), where $\square$ indicates a vacancy arising from the absence of a Ca^{2+} ion, and the distances from the two Gd^{3+} ions to the vacancy maybe unequal (see below). As discussed above, the Gd^{3+} ions in center "b" is thought to correspond to occupation at the Ca1 sites. An interesting question that then arises is the likely location of $\square$. A location of the vacancy at the nearest Ca1 neighbor (i.e., $Ca1^1$ at z = 1/2) is unlikely, because this arrangement would have preserved the triad axis of the ideal Ca1 site, inconsistent with the rhombic feature of the observed D matrix or the results of the pseudo-symmetry analysis. A possible model is that this vacancy is located at the Ca2 neighbor site nearest to a Gd^{3+}-substituted Ca1 site (e.g., $Ca1^1$ -- $Ca2^1$; Fig. 1).

The location of the vacancy associated with the Gd^{3+}-occupied Ca1 site, at the nearest Ca2 site, is supported both by the principal directions of the observed matrix **D** and by the results of the pseudo-symmetry analysis. The coordination polyhedron of the ideal Ca1 site in fluorapatite is elongated parallel to the crystallographic c axis and this closely matches the measured direction $\mathbf{D}_3$. The (small) deviation of $\mathbf{D}_3$ from the c axis (Table 3) probably is caused by the vacancy at the nearest Ca2 site. Such a vacancy would cause a substantial displacement of atom $O3^H$ (that is shared by $Ca1^1$ and $Ca2^1$; Fig. 1) away from the $Ca2^1$ site toward the $Ca1^1$ site. This distortion can readily explain the deviation of the D_3 direction from the crystallographic c axis and the large differences in the fitted D_1 and D_2 values (D_1/D_2 = 13; Table 3), which would be expected to be equal for the ideal Ca1 site (Hughes et al. 1989). Also, the displacement in $O3^H$ results in replacement of the vertical threefold rotation axis at the ideal Ca1 site (Hughes et al. 1989) by an approximate horizontal mirror plane for the center "b," which is equivalent to the approximately vertical twofold pseudo-symmetry axis revealed by the pseudo-symmetry analysis (Fig. 8). The principal $\mathbf{D}_3$ direction also matches the expectation of the superposition model (Brodbeck and Bukrey 1981; Kliava 1982; Gaite et al., 1985; Mombourquette and Weil 1987), which suggests that direction $\mathbf{D}_3$ reflects the elongation of the coordination polyhedron within which the paramagnetic ion resides.

The location of the second Gd^{3+} ion in the proposed Gd^{3+} -- $\square$ --- Gd^{3+} arrangement remains uncertain but this cation must be well separated from the first Gd^{3+} ion, on the basis of absence of any observed magnetic dipolar interactions between neighboring Gd^{3+} ions. Note that the location of the vacancy at a neighboring Ca2 site is expected to lead to slightly different distortions of the two Gd^{3+}-occupied Ca1 sites, and hence different principal directions for their D matrices. This effect may explain the broader inherent line width of the W-band EPR spectra for Gd^{3+} at the Ca1 sites, as compared to that of Gd^{3+} at the Ca2 sites, which does not involve any vacancy and hence shows no such effect.

Comparison of the two Gd^{3+} centers in fluorapatite

The D and E values of center "b" at the Ca1 sites are significantly larger than those of center "a" at the Ca2 sites (Table 3), although both these Gd^{3+} centers have rhombic local symmetry. Hughes et al. (1989) pointed out that the ideal Ca2 site is an approximate CaO_5F octahedron, although a weak Ca2-O1 bond also exists. Chen et al. (2002) showed that the substitution of Gd^{3+} into a Ca2 site is accompanied by a replacement of F^- by O^{2-}, which may have increased the resemblance of the Ca2 polyhedron to an octahedron. The ideal CaO_9 polyhedron at the Ca1 sites, on the other hand, is highly elongated along the c axis (Hughes et al. 1989). Moreover, the involvement of a vacancy in the incorporation of Gd^{3+} into the Ca1 sites also introduces substantial distortions. Therefore, the larger D and E values of center "b" at the Ca1 sites compared to "a" at the Ca2 sites presumably are attributable to differences in the local symmetries of the ideal Ca1 and Ca2 sites and to the distortions introduced by the incorporation of Gd^{3+}.

The relative abundance of the two Gd^{3+} centers at the Ca1 and Ca2 sites in fluorapatite has been estimated by simulation of the W-band single-crystal spectrum at $\mathbf{B}\|\mathbf{z}'$ and $\mathbf{B}_1\|\mathbf{x}'$. First each "allowed" transition from the two Gd^{3+} centers was simulated separately, with lorentzian line shape but different line widths. Then the lines from the different transitions were summed to obtain the two spectra from the Gd^{3+} centers at the Ca1 and Ca2 sites. Finally the two spectra were added together by trial and error using different intensity ratios to match the measured spectrum (Fig. 3a). The intensity ratio between the two Gd^{3+} centers at the Ca1 and Ca2 sites was found to be 3.42, corresponding to a site-occupancy ratio (Gd-Ca2/Gd-Ca1) of 0.2, because the multiplicities of the Ca1 and Ca2 sites are 4 and 6, respectively. This site-occupancy ratio is significantly lower than that of a Gd-rich fluorapatite (10.36 wt% Gd_2O_3) from X-ray structure refinement (Gd-Ca2/Gd-Ca1 = 2.0; Fleet and Pan 1995). We tenatively attribute the difference in the calculated site occupancy ratios to: (1) much lower temperature (~700 °C) used in the hydrothermal synthesis of the latter, and (2) the presence of charge-compensating Na^+ and Si^{4+} ions for the incorporation of Gd^{3+} in the Gd-rich fluorapatite (Fleet and Pan 1995).

ACKNOWLEDGMENTS

We thank A.M. Hofmeister, J. Rakovan, and an anonymous referee for constructive reviews and helpful suggestions. We also wish to thank W.C. Tennant for providing the computer program ROTSTO and for numerous helpful comments, R.L. Belford, and A. Smirnov for hospitality and beneficial discussions at IERC, and the Natural Sciences and Engineering Research Council (NSERC) of Canada, as well as the U.S. National Institutes of Health (NIH: RR01811) for financial support.

Brought to you by | University of Toronto-Ocul
Authenticated
Download Date | 12/1/15 12:10 PM

REFERENCES CITED

Al'tshuler, S.A. and Kozyrev, B.M. (1974) Electron paramagnetic resonance in compounds of transition elements, 2nd rev. ed., 589 p. Halstead-Wiley, New York.

Brodbeck, C.M. and Bukrey, R.R. (1981) Model calculations for the coordination of Fe^{3+} and Mn^{2+} ions in oxide glasses. Physical Review B, 24, 2334–2342.

Chen, N., Pan, Y., and Weil, J.A. (1999) Single-axis crystal holder for EPR work, and use of powdered DPPH as a *g*-standard. EPR Newsletter of the International EPR (ESR) Society, 10, 6–7.

———(2002) Electron paramagnetic resonance spectroscopic study of synthetic fluorapatite: Part I. Local structural environment and substitution mechanism of Gd^{3+} at the Ca2 site. American Mineralogist, 87, 37–46**.**

Cheburkin, A.K., Frei, R., and Shotyk, W. (1997) An energy-dispersive miniprobe multielement analyzer (EMMA) for direct analysis of trace elements and chemical age dating of single mineral grains. Chemical Geology, 135, 75–87.

Comodi, P., Liu, Y., Stoppa, F., and Woolley, A.R. (1999) A multi-method analysis of Si-, S- and REE-rich apatite from a new kind of kalsilite-bearing leucitite (Abruzzi, Italy). Mineralogical Magazine, 63, 661–672.

Fleet, M.E. and Pan, Y. (1995) Site preference of rare-earth elements in fluorapatite. American Mineralogist, 80, 329–335.

———(1997) Rare-earth elements in apatite: Uptake from H_2O-bearingphosphate-fluoride melts and the role of volatile components. Geochimica et Cosmochimica Acta, 61, 4745–4760.

Fleet, M.E. Liu, X., and Pan, Y. (2000a) Rare-earth elements in chlorapatite $[Ca_{10}(PO_4)_6Cl_2]$: uptake, site preference and degradation of monoclinic structure. American Mineralogist, 85, 1437–1446.

——— (2000b) Site preference of rare-earth elements in hydroxyapatite $[Ca_{10}(PO_4)_6(OH)_2]$. Journal of Solid State Chemistry, 149, 391–398.

Gaite, J.M. (1980) Pseudo-symmetries of crystallographic coordination polyhedra. Application to forsterite and comparison with some EPR results. Physics and Chemistry of Minerals, 6, 9–17.

———(1987) Study of the structural distortion around S-state ions in crystals, using the fourth-order spin-Hamiltonian term of the EPR spectral analysis. In Electronic Magnetic Resonance of the Solid State, Weil, J. A., Ed., Canadian Society of Chemistry, Ottawa, ON, Canada, 151–174.

Gaite, J.M., Bulka G.R., Hasanova, N.M., Nizamutdinov, N.M., and Vinokurov, V.M. (1985) EPR of Gd^{3+} in $Na_2Cd(SO_4)_2 2H_2O$, comparison with previous results obtained for Fe^{3+}. Journal of Chemical Physics, 83, 6088–6090.

Hughes, J.M., Cameron, M., and Crowley, K.D. (1989) Structural variations in natural F, OH and Cl apatites. American Mineralogist, 74, 870–876.

Hughes, J.M., Cameron, M., and Mariano, A.N. (1991) Rare-earth element ordering and structural variations in natural rare-earth bearing apatites. American Mineralogist, 76, 1165–1173.

Kliava, J. (1982) Superposition model analysis of the short-range ordering for Mn^{2+} in oxide glasses. Journal of Physics C: Solid State Physics, 15, 7017–7029.

Michoulier, J. and Gaite, J.M. (1972) Site assignment of Fe^{3+} in low-symmetry crystals. Application to $NaAlSi_3O_8$. Journal of Chemical Physics, 56, 5205–5213.

Mombourquette, M.J. and Weil, J.A (1987) Modeling Fe^{3+} in quasitetrahedral surroundings using the Newman superposition model. Journal of Chemical Physics, 87, 3385–3391.

Mombourquette, M.J., Tennant,W.C., and Weil, J.A. (1986) EPR study of Fe^{3+} in α-quartz: a reexamination of the so-called *I* centre. Journal of Chemical Physics, 85, 68–79.

Mombourquette, M.J., Weil, J.A., and McGavin, D.G. (1996) EPR-NMR User's Manual. Department of Chemistry, University of Saskatchewan, Canada.

Nilges, M.J., Smirnov, A.I., Clarkson, R.B., and Belford, R.L. (1999) Electron paramagnetic resonance W-band spectrometer with a low-noise amplifier. Applied Magnetic Resonance, 16, 167–183.

Pan, Y. and Breaks, F.W. (1997) Rare-earth elements in fluorapatite, Separation Lake area, Ontario: Evidence for S-type granite–rare-element pegmatite linkage. Canadian Mineralogist, 35, 659–671.

Pan, Y., Fleet, M.E., and MacRae, N.D. (1993) Oriented monazite inclusions in apatite porphyroblasts from the Hemlo gold deposit, Ontario, Canada. Mineralogical Magazine, 57, 697–707.

Tennant, W.C., Walsby, C.J., Claridge, R.F.C., and McGavin, D.G. (2000) Rotation matrix elements and further decomposition functions of two-vector tesseral spherical tensor operators; their uses in electron paramagnetic resonance spectroscopy. Journal of Physics: Condensed Matter, 12, 9481–9495.

Weil, J.A., Bolton, J.R., and Wertz, J.E. (1994) Electron paramagnetic resonance, Elementary theory and practical applications, 568 p. Wiley-Interscience, New York.

MANUSCRIPT RECEIVED DECEMBER 15, 2000
MANUSCRIPT ACCEPTED AUGUST 10, 2001
MANUSCRIPT HANDLED BY ANNE F. HOFMEISTER

Brought to you by | University of Toronto-Ocul
Authenticated
Download Date | 12/1/15 12:10 PM